Transonic Wing Design Using Inverse Methods in Curvilinear Coordinates

Thomas A. Gally* and Leland A. Carlson†
Texas A&M University, College Station, Texas

An inverse wing design method has been developed around an existing transonic wing analysis code. The original analysis code, TAWFIVE, has as its core the numerical potential flow solver FLO30, developed by Caughey and Jameson. Features of the analysis code include a finite-volume formulation, an SLOR solution scheme, and a wing and fuselage fitted, curvilinear grid mesh. The development of the inverse method as an extension of previous methods existing for design in Cartesian coordinates is presented. Results are shown for inviscid wing design cases in supercritical flow regimes. The test case selected also demonstrates the versatility of the design method in designing an entire wing or discontinuous sections of a wing.

Nomenclature

c = chord length
C_p = coefficient of pressure
h = Jacobian of coordinate transformation
$\mathbf{H}$ = Jacobian matrix
J = transpose of inverse Jacobian matrix
M_∞ = freestream Mach number
P,Q,R = upwinding terms
$Q_{ij}, Q_{i,j,k}$ = decoupling terms
q = magnitude of local velocity vector
q_∞ = magnitude of freestream velocity vector
S = wing surface function
u,v,w = components of physical velocity vector
U,V,W = components of contravariant velocity vector
V = contravariant velocity vector
x,y,z = Cartesian coordinate directions
α = angle of attack
γ = ratio of specific heats
δ = differential operator
$\delta(x)$ = displacement thickness
$\delta_r(x)$ = displacement thickness due to relofting
Δ = trailing-edge thickness
Δ_t = user-specified trailing-edge thickness
ϵ = decoupling factor
μ = averaging operator
ξ,η,ζ = curvilinear coordinate directions
ρ = density
ϕ = reduced/perturbation potential function
Φ = potential function ($\Phi=\phi+x\cos\alpha+y\sin\alpha$)

Introduction

In recent years, the importance of transonic flight to both military and commercial aircraft and the development of specialized transonic wings for several flight research experiments have prompted significant efforts to develop accurate and reliable computational methods for the analysis and design of transonic wings. Many methods of solution have been developed, but among those that have shown promise due to their computational efficiency and engineering accuracy have been those based upon the full potential flow equations in either their conservative or nonconservative form.[1-3] The TAWFIVE[4] code in particular has proven to be an excellent and reliable analysis tool. This code is based upon the FLO30 finite-volume potential flow method that was developed by Caughey and Jameson.[3] Among the features of FLO30 are its fully conservative formulation and its three-dimensional curvilinear grid. The latter can be fit around any general combination of fuselage shape and wing planform.

The purpose of the research described in this paper has been to develop a wing design method that is based on the existing TAWFIVE analysis code and is compatible with the existing computational methods and program structure of that code. Of the many wing and airfoil design methods available,[5-8] the inverse method as developed by Carlson,[9,10] Anderson and Carlson,[11] and Weed et al.[12] was selected for use. The current work extends the previously developed design methods developed for orthogonal grids to the more generalized curvilinear grid system of TAWFIVE, while also providing greater design flexibility and versatility for engineering applications. These last goals were achieved by the inclusion of user options for designing either the entire wing or only discontinuous wing segments as shown in Fig. 1. The availability of this option is useful to engineers who are typically faced with designing around regions where the wing geometry may be fixed by constraints other than aerodynamic considerations.

Wing Analysis Methods

Potential Flow Solver

The inviscid potential analysis of TAWFIVE is performed by the program FLO30 developed by Caughey and Jameson.[3,13] For a complete description of the FLO30 code and its theoretical basis, the reader is referred to Caughey and Jameson's papers and some earlier developmental work by Jameson.[14,15] A brief description is presented here to provide for completeness and a background for the inverse design developments that will be discussed in detail.

FLO30 solves the full potential equation in conservative form that when transformed from Cartesian coordinates to generalized curvilinear coordinates is

$$(\rho hU)_\xi + (\rho hV)_\eta + (\rho hW)_\zeta = 0 \tag{1}$$

where the subscripts denote differentiation with respect to the curvilinear coordinates ξ,η, and ζ. The contravariant velocities are related to the physical velocities and the derivatives of the potential function by

$$\begin{bmatrix} U \\ V \\ W \end{bmatrix} = \mathbf{H}^{-1} \begin{bmatrix} u \\ v \\ w \end{bmatrix} = [\mathbf{H}^T\mathbf{H}]^{-1} \begin{bmatrix} \Phi_\xi \\ \Phi_\eta \\ \Phi_\zeta \end{bmatrix} \tag{2}$$

Presented as Paper 87-2551 at the AIAA 5th Applied Aerodynamics Conference, Monterey, CA, Aug. 17-19, 1987; received Sept. 11, 1987; revision received Oct. 27, 1987.

*Graduate Research Assistant.
†Professor of Aerospace Engineering. Associate Fellow AIAA.

where H is the transformation matrix defined by

$$\mathrm{H}=\begin{bmatrix} x_\xi & x_\eta & x_\zeta \\ y_\xi & y_\eta & y_\zeta \\ z_\xi & z_\eta & z_\zeta \end{bmatrix} \tag{3}$$

with $h=|\mathrm{H}|$. An equation for the local density can be obtained from isentropic relations as

$$\rho=\left[1+\frac{\gamma-1}{2}M_\infty^2(1-u^2-v^2-w^2)\right]^{1/(\gamma-1)} \tag{4}$$

The numerical approach used in FLO30 is a finite-volume technique. To understand this approach, consider the simple two-dimensional case represented by the grid system shown in Fig. 2. The dashed cube shown in the figure indicates the area element under consideration. The flux of fluid through side a-b can be approximated by the average of the fluxes at point a and b with similar results for the side c-d. The net flux in the x direction for the elemental area centered at grid point i,j is then

$$(\rho hU)_\xi=\frac{[(\rho hU_a+\rho hU_b)-(\rho hU_c+\rho hU_d)]}{2\Delta\xi} \tag{5}$$

or, in the notation of Caughey and Jameson,

$$(\rho hU)_\xi=\mu_\eta\delta_\xi(\rho hU) \tag{6}$$

where δ and μ are differentiating and averaging operators in the indicated directions that are defined as follows (allowing $\Delta\xi=\Delta\eta=\Delta\zeta=1$):

$$(\delta_\xi u)_{i,j,k}=(U_{i+\frac{1}{2},j,k}-U_{i-\frac{1}{2},j,k}) \tag{7a}$$

$$(\mu_\xi U)_{i,j,k}=(U_{i+\frac{1}{2},j,k}+U_{i-\frac{1}{2},j,k})/2 \tag{7b}$$

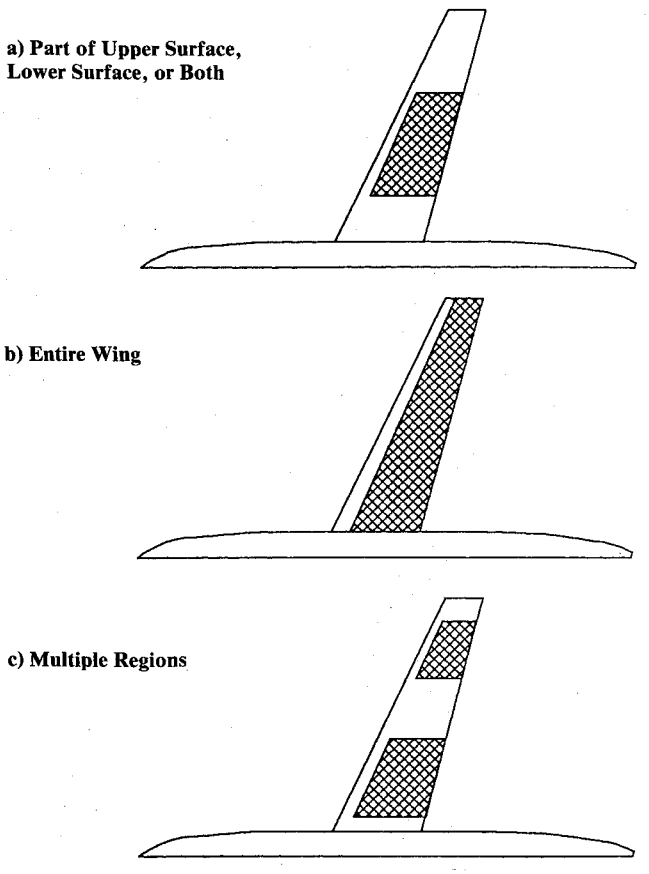

Fig. 1 Possible wing design situations.

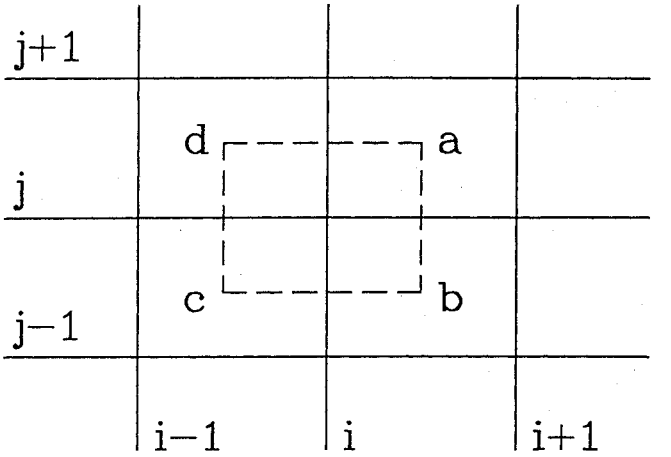

Fig. 2 Finite-volume cell location.

$$(\mu_{\xi\eta}U)_{i,j,k}$$
$$=(U_{i+\frac{1}{2},j+\frac{1}{2},k}+U_{i+\frac{1}{2},j-\frac{1}{2},k}$$
$$+U_{i-\frac{1}{2},j+\frac{1}{2},k}+U_{i-\frac{1}{2},j-\frac{1}{2},k})/4 \tag{7c}$$

When extended to the other flux components and to averaging over cube surfaces in three dimensions, the numerical potential equation is of the form

$$\mu_{\eta\zeta}\delta_\xi(\rho hU)+\mu_{\zeta\xi}\delta_\eta(\rho hV)+\mu_{\xi\eta}\delta_\zeta(\rho hW)=0 \tag{8}$$

To find the flux quantities ρhU, ρhV, and ρhW at the finite-volume cell vortices (i.e., points a, b, c, and d for the two-dimensional case), it is necessary to evaluate Eqs. (2-4). The derivatives in these expressions can be expanded by the same volume averaging approach used above, thus

$$\Phi_\xi=\mu_{\eta\zeta}\delta_\xi(\Phi) \qquad x_\xi=\mu_{\eta\zeta}\delta_\xi(x) \tag{9a}$$

$$\Phi_\eta=\mu_{\zeta\xi}\delta_\eta(\Phi) \qquad y_\xi=\mu_{\eta\zeta}\delta_\xi(y) \tag{9b}$$

$$\Phi_\zeta=\mu_{\xi\eta}\delta_\zeta(\Phi) \qquad z_\xi=\mu_{\eta\zeta}\delta_\xi(z) \tag{9c}$$

with similar terms for the other transformation metrics. The above expressions, being centered at grid midpoints, will involve the values at grid points of the potential and grid position, which are known from the previous potential solution and the grid geometry, respectively.

When solving transonic flows, it is necessary to include some form of supersonic upstream dependence and artificial viscosity in the solution algorithm in order to account for the physical nature of the flow and the viscous nature of shock waves, respectively. Caughey and Jameson introduced upwinding by the addition of terms into their potential numerical equations that are only nonzero when the flow is supersonic. These terms also introduce a numerical error that has the form of a viscous term. Additional terms are also included to correct a tendency of the flowfield solution to uncouple between alternating grid points. The final numerical equation, which is solved by FLO30 when these terms have been included, has the form

$$\mu_{\eta\zeta}\delta_\xi(\rho hU+P)+\mu_{\zeta\xi}\delta_\eta(\rho hV+Q)$$
$$+\mu_{\xi\eta}\delta_\zeta(\rho hW+R)-\epsilon(\mu_\zeta\delta_{\xi\eta}Q_{\xi\eta}+\mu_\xi\delta_{\eta\zeta}Q_{\eta\zeta}$$
$$+\mu_\eta\delta_{\zeta\xi}Q_{\zeta\xi}-\delta_{\xi\eta\zeta}Q_{\xi\eta\zeta}/2)=0 \tag{10}$$

where P, Q, and R are the upwinding terms; $Q_{\epsilon\eta}$, $Q_{\eta\zeta}$, $Q_{\zeta\xi}$, and $Q_{\xi\eta\zeta}$ are the terms reducing odd-even decoupling; and ϵ is a factor determining the amount of decoupling (typically $\epsilon=0.25$).

Computational Grid Geometry

The computational grid used by FLO30 is a body-fitted, nonorthogonal, curvilinear mesh constructed about a wing/fuselage combination. The number of grid points composing the computational domain is typically $40\times6\times8$, $80\times12\times16$, or $160\times24\times32$ for the number of ξ, η, and ζ points in the coarse, medium, and fine grids, respectively. The grid is conformally mapped to the wing and fuselage surfaces as can be seen from the plot of surface grid lines shown in Fig. 3.

The grid is formed around spanwise airfoil sections in a similar manner in which "C" grids are mapped to airfoils in two-dimensional analysis. In addition, each spanwise computational plane is also conformally wrapped about the fuselage surface and a line extending forward from the fuselage nose. The reader is referred to Refs. 3 and 13 for additional details on the method of grid generation.

An additional set of grid surfaces are generated beneath the wing and fuselage surfaces and beyond the symmetric plane in order to aid in the formulation of both the finite-volume numerical flow equations and the flow tangency boundary conditions on these boundaries. The grid points composing the "ghost" surfaces are calculated from linear extrapolations of the computation grid lines from inside the physical domain.

Boundary Conditions

Since the governing potential equations are written in terms of perturbations from freestream conditions, the subsonic, far-field requirement that the flow return to the freestream velocity and direction is satisfied by setting the perturbation potential equal to zero on the side and upstream boundaries. The downstream boundary condition is a "zero"-order extrapolation of the potential (constant potential assumption) to the outflow boundaries.

A flow tangency condition is applied along both the wing and fuselage solid surfaces by setting the normal contravariant component of the velocity vector to zero on the surfaces. This condition provides an equation that, when approximated by a finite-difference expansion about the surface grid points, can be used to set a value for the perturbation potential on the "ghost" grid points below each surface. Note that this finite-difference boundary condition differs in formulation from the finite-volume solution algorithm of the governing equations. As a result, it would be possible to impose flow tangency using the finite-difference technique yet still have a slight normal surface velocity when performing the finite-volume calculations. Since it is essential to have accurate boundary conditions at the wing surface in order to generate accurate solutions, a second condition is imposed on the wing surface. This additional condition involves reflecting the flux quantities calculated by the flow solver for the cell centers directly above the wing surface to the "ghost" cell centers beneath. The reflected normal fluxes then cancel each other out in the residual expression and a net zero flow is obtained through the surface. Similarly, a zero flux condition is applied at the half-body symmetric plane, limiting solutions to symmetric, nonsideslip cases.

The trailing-edge slit boundary separating the upper and lower half planes is not an actual limit to the physical domain as the other boundaries are, but is simply an artificial boundary created by unwrapping the physical plane into the computational domain. The only conditions that need to be imposed at the slit are that the flow velocities, and thus pressure, be continuous across the cut. The flow potential, however, will have a discontinuous jump across the wake that is proportional to the sectional wing lift coefficient.

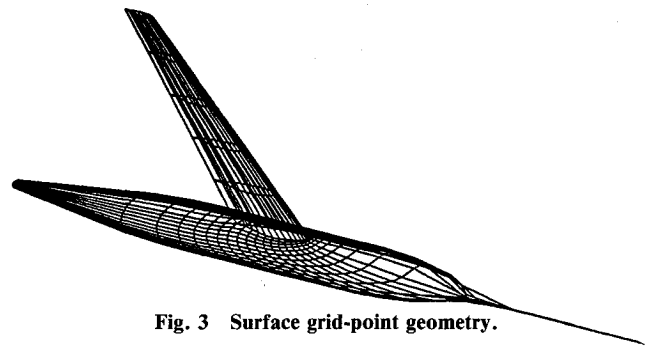

Fig. 3 Surface grid-point geometry.

Inverse Wing Design Methods

As stated previously, a direct-inverse approach to wing design was selected for incorporation into the TAWFIVE code. The direct-inverse method derives its name from the division of the design wing surface into a fixed geometry leading-edge region, where flow tangency boundary conditions are imposed, and an aft, variable geometry section where pressure boundary conditions are enforced. The pressure boundary where the user-specified pressure distributions are imposed does not extend forward to the leading edge due to difficulties of enforcing this type of boundary condition near the beginning of an airfoil section. This restriction on the size of the pressure specification region does not seriously reduce the versatility of the design method since the direct region can be fairly small (as little as 3% chord), the leading-edge regions for most airfoils are geometrically similar, and it is relatively easy to select a leading-edge geometry that will produce the desired Mach number or pressure values at the beginning of the inverse region. In addition, specific leading-edge shapes may be required due to other design constraints such as the necessity to house a leading-edge flap or slat system.

Pressure Boundary Condition

In the inverse design regions on the wing, a pressure boundary condition will be specified rather than the flow tangency condition used in analysis zones. In formulating this boundary condition, it is necessary to relate the user-specified pressure coefficient C_p, to the current perturbation potentials at inverse design grid points. Consider the full potential equation for the pressure coefficient:

$$C_p=\frac{2}{\gamma M_\infty^2}\left\{\left[1+\frac{\gamma-1}{2}M_\infty^2\left(1-\frac{q^2}{q_\infty^2}\right)\right]^{\gamma/(\gamma-1)}-1\right\} \tag{11}$$

where $q^2=u^2+v^2+w^2$.

If it is assumed that the pressure coefficient is primarily a function of the chordwise component of the velocity u and only slightly affected by the vertical and spanwise components of velocity v and w, then a stable approximation is made by time lagging the latter two velocities in the boundary condition expression. This assumption is true everywhere except near the leading edge; but since the inverse design boundaries have already been restricted to regions behind the leading edge, the simplification is justified. The value of the local velocity u can then be calculated from the above expession in terms of the desired pressure coefficient and the current values for the vertical and spanwise velocities. In addition, the velocity u can also be calculated from the perturbtion potentials using the relations of Eq. (2). Defining J_{ij} to be the elements of the inverse transpose of the Jacobian matrix H, the two equations for u yield:

$$J_{11}\phi_\xi+J_{12}\phi_\eta+J_{13}\phi_\zeta=\left[\frac{1-\frac{2}{(\gamma-1)M_\infty^2}\left[\left(1+\frac{\gamma M_\infty^2 C_p}{2}\right)^{\frac{\gamma-1}{\gamma}}-1\right]}{1+\left(\frac{v}{u}\right)^2+\left(\frac{w}{u}\right)^2}\right]^{1/2}-\cos\alpha \tag{12}$$

Since the spanwise and vertical flow velocities have already been assumed to be constant in the boundary condition relation, it is consistent to make the same approximation in the above expression with respect to the spanwise and vertical derivative terms ϕ_η and ϕ_ζ. This assumption is similar to the previous one, and leads to an explicit expression for the potential at one point.

The finite-difference approximation used involves expanding the derivatives of the potential about the midpoint $i-\frac{1}{2}, j, k$. The ξ derivative is determined by a central difference involving the preceding and following grid point values. The η and ζ derivatives are found at the midpoint by averaging the derivatives from the preceding and following grid points found by three-point-backwards and central-difference approximations, respectively. Figure 4 shows the point dependence and pressure specification point for this method. The resulting numerical expression obtained with these finite approximations is:

$$\begin{aligned} &J_{11}(\phi^{n+1}_{i,j,k}-\phi^{n}_{i-1,j,k}) \\ &+J_{12}[3(\phi^{n+1}_{i,j,k}+\phi^{n}_{i-1,j,k})-4(\phi^{n}_{i,j-1,k}+\phi^{n}_{i-1,j-1,k}) \\ &+\phi^{n}_{i,j-2,k}+\phi^{n}_{i,1,j-2,k}]/4 \\ &+J_{13}(\phi^{n}_{i,j,k+1}+\phi^{n}_{i-1,j,k+1}-\phi^{n}_{i,j,k-1}-\phi^{n}_{i-1,j,k-1})/4 \\ &=F(C_{p,i-\frac{1}{2},k}) \end{aligned} \tag{13}$$

Here, the superscripts n and $n+1$ refer to current values of the potential and the new values of the potential being imposed by the boundary condition, respectively. Also, the term $F(C_{p,i-\frac{1}{2},k})$ is the right-hand side of Eq. (12) evaluated using the pressure coefficient specified at point $i-\frac{1}{2}, k$. Solving the above expression for the potential at point i,j,k yields

$$\begin{aligned} \phi^{n+1}_{i,j,k}=&\frac{1}{J_{11}+\frac{3}{4}J_{12}}\{J_{11}\phi^{n}_{i-1,j,k} \\ &-J_{12}[3\phi^{n}_{i-1,j,k}-4(\phi^{n}_{i,j-1,k}+\phi^{n}_{i-1,j-1,k}) \\ &+\phi^{n}_{i,j-2,k}+\phi^{n}_{i-1,j-2,k}]/4 \\ &-J_{13}(\phi^{n}_{i,j,k+1}+\phi^{n}_{i-1,j,k+1}-\phi^{n}_{i,j,k-1} \\ &-\phi^{n}_{i-1,j,k-1})/4+F(C_{p,i-\frac{1}{2},k})\} \end{aligned} \tag{14}$$

The potential values at $n+1$ in the direct region are known initially since they do not change when the inverse boundary condition is applied; i.e., $\phi^{n+1}=\phi^{n}$. All the potentials on the inverse boundary can then be calculated and, since the spanwise and vertical derivatives are small, will primarily be functions of the pressure coefficient at grid point $i-\frac{1}{2}$ and the value of the potential at grid point $i-1$.

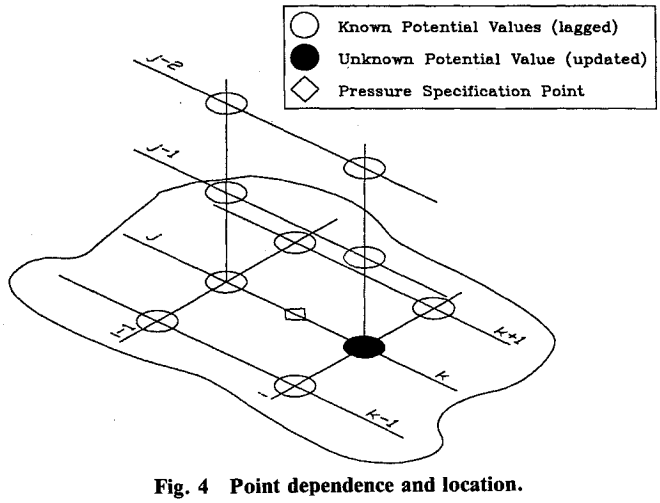

Fig. 4 Point dependence and location.

Surface Calculations

As the inverse boundary conditions drive the flowfield to a converged solution, it is necessary to calculate periodically the location of the new displacement surface and to regenerate the computational grid about this new geometry so that the pressure boundary surface will correspond to the physical boundary surface being designed. Each new surface is found relative to the previous surface from an integration of the wing surface slopes. The surface slopes are calculated from the current flowfield solution using the flow tangency boundary condition, which in curvilinear coordinates is

$$V^T\times\nabla S=0 \tag{15}$$

Note this condition, with the gradient in the curvilinear plane, is a direct analog to the same condition expressed in the physical plane.

A more useful expression can be obtained by expanding the above equation to:

$$\left(\frac{\partial\eta}{\partial\xi}\right)_{\text{wing}}=\frac{V}{U}-\frac{W}{U}\left(\frac{\partial\eta}{\partial\zeta}\right)_{\text{wing}} \tag{16}$$

This expression can be solved for the new chordwise airfoil slope $\partial\eta/\partial\xi$ if the current values of the spanwise slope $\partial\eta/\partial\zeta$ are used. Since the wing surface is represented in the computational grid as a plane of constant η, the current slopes on the wing surface equal zero and a simplified flow tangency condition results:

$$(\partial\eta/\partial\xi)_{\text{wing}}=V/U \tag{17}$$

The above expession has been applied to the computational surface plane in order to find the relative location of the new physical surface. This approach is an approximation, since the above equation is only exactly true when applied to the new surface itself. Using this method, however, provides for a stable iterative surface updating procedure that quickly converges[6] to the target surface.

To calculate the relative surface slopes, it is first necessary to determine accurately the values of the contravariant velocities, U and V. As was also determined by the work of Weed et al.,[12] a simple finite-difference calculation of these velocities is not sufficiently accurate. Borrowing from Ref. 12, a more accurate method was implemented that uses the residual expression to calculate the velocity ratio V/U, under the assumption that the residual is zero at the surface points. The residual expression from FLO30 can be written in finite-volume form as

$$\begin{aligned} &\mu_{\eta\zeta}\delta_\xi(\rho hU)+\mu_{\zeta\xi}\delta_\eta(\rho hV)+\mu_{\xi\eta}\delta_\zeta(\rho hW) \\ &+(\text{other terms})=0 \end{aligned} \tag{18}$$

The "other terms" in Eq. (18) involve the grid point coupling and upwind dependence terms of the formulation and are assumed to be constants in the following development.

The desired velocities can also be written in this finite volume form as:

$$\frac{V}{U}=\frac{\rho hV}{\rho hU}=\frac{\mu_{\xi\eta\zeta}(\rho hV)}{\mu_{\xi\eta\zeta}(\rho hU)} \tag{19}$$

By simple manipulations, the normal velocity can be obtained from the residual expression as

$$\begin{aligned} &2\mu_{\xi\eta\zeta}(\rho hV)=2\mu_{\zeta\xi}(\rho hV)_{\eta-1}-\mu_{\eta\zeta}\delta_\xi(\rho hU) \\ &-\mu_{\xi\eta}\delta_\zeta(\rho hW)-(\text{other terms}) \end{aligned} \tag{20}$$

where the subscript $\eta-1$ refers to the values at grid cell centers above the wing surface.

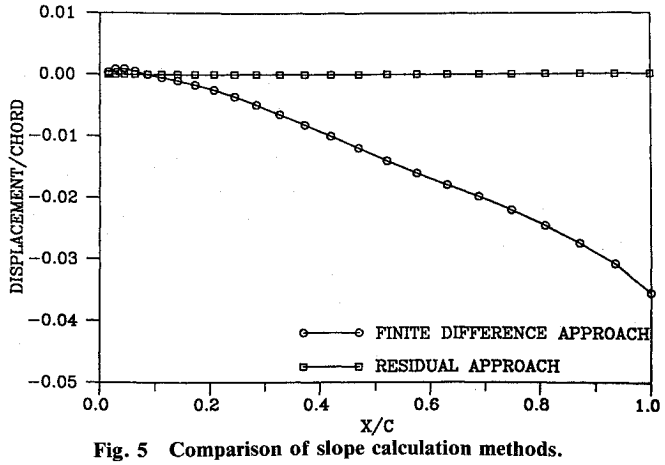

Fig. 5 Comparison of slope calculation methods.

In order to use Eq. (20) to find the desired surface velocity ratio, it is necessary to know the U and W velocity components at the "ghost" cell centers below the wing surface. These values can be obtained in a manner consistent with FLO30 by specifying the "ghost" cell values to equal the values at corresponding points immediately above the wing surface. A comparison of the accuracy of both the finite-difference approach and residual approach is shown in Fig. 5. The calculated displacements are for a converged analysis solution for which the calculated slopes should, of course, be zero.

With the contravariant velocities known, an integration of Eq. (17) in the chordwise direction ξ from the start of the inverse region to the trailing edge yields a set of surface displacements for the new wing surface relative to the previous one. These displacements are expressed as changes in the computational coordinate η and are converted to surface displacements in the physical plane $\delta(x)$ via the local grid transformation. The physical plane displacements are coincident with the computational grid points in the inverse regions. To obtain the corresponding displacements at the original geometrical locations specified in the program input data, a linear interpolation of the above data is performed. Finding the displacements at the original geometry stations permits the calculation of the new wing airfoil sections at the same semispan locations.

Trailing-Edge Closure

The procedures outlined above will compute a wing surface corresponding to a given, fixed, leading-edge geometry and to a desired set of pressure distributions in the inverse regions. The above procedures do not, however, guarantee that this wing geometry will be practical. In particular, past experience[9] has shown that inverse surface calculations may yield airfoil sections that have either excessively blunt trailing edges or which, at least numerically, have the upper and lower surface crossed at the trailing edge ("fish tailed"). The former case is undesirable due to aerodynamic considerations, while the latter is physically impossible and may produce unpredictable problems in the grid generation or flow calculation portions of FLO30.

Since for any specified pressure distribution the corresponding wing surface will be controlled by the leading-edge geometry, which serves as an initial spatial boundary condition for the inverse region, the problem of assuring trailing-edge closure can be viewed as the proper selection of a leading-edge shape. A procedure for systematically modifying the leading-edge region in order to achieve some desired trailing-edge thickness is called relofting. Such a relofting procedure has been incorporated into the present design process in order both to prevent the problems of trailing-edge crossover and to allow the user the option of specifying a trailing-edge thickness as an additional design variable. This design feature should be very useful in practical applications since it automates the iterative selection of a leading-edge shape that would otherwise have to be performed by the user.

Two methods of relofting can presently be selected. The first method is a simple linear rotation scheme. This method can be visualized with the help of Fig. 6. The dashed line indicates the original leading-edge geometry and a hypothetical new surface shape that has been calculated for the inverse design regions. Without modification, this new surface has a trailing-edge thickness of Δ. If a thickness of Δ_t were specified by the user, then the surface would have to be relofted or changed. In the present scheme, in order to obtain the desired thickness, a displacement thickness δ_t is added to the current design surface. This thickness has a distribution from the leading to the trailing-edge and is determined by the formula

$$\delta_t(x) = (\Delta_t - \Delta)(x/c) \tag{21}$$

where c is the chord length of the local airfoil section. The total displacement for a surface update is then the sum of the two displacements $\delta(x)$ and $\delta_t(x)$. When both the upper and lower surfaces are designed simultaneously, the displacement magnitudes determined by relofting are divided between the two surfaces so that half is added to the lower surface and half to the upper surface.

The second relofting method uses the same approach as the first for the aft inverse regions, but modifies the leading-edge region by a proportional thining or thickening of the surface ordinates. This approach can be expressed by:

$$y^{n+1}(x) = y_y^{n+1}[y^n(x)/y_j^n] \tag{22}$$

here the j subscript refers to the ordinate at the direct-inverse junction determined from the linear relofting of the aft regions. Note that this method will produce leading edges in the same family of shapes and, for example, allow the design of an NACA 0006 airfoil when starting from an NACA 0012 airfoil (see test case II).

Results

A variety of different test cases were run as verification of the current design method. These cases involved both subcritical design and supercritical design over section geometries selected to test the versatility of the input and design control logic. In this section, results from two of the more significant test cases will be presented. The results shown were obtained on a medium grid having 81 streamwise, 13 vertical, and 19 spanwise points with 11 spanwise stations and 53 points on the wing at each station; and, in all cases, the maximum change in the reduced potential was reduced at least three orders of magnitude. Thus, the results do not represent ultimate convergence but should be representative of "engineering accuracy."

The use of the medium grid for the design cases shown in the following was dictated by computational cost and time. Fine grid solutions for these type geometries have been obtained but are not significantly different from the medium grid results except for a generally smoother shape. Use of the fine grid in design is necessary, however, when the airfoil sections involved are aft cambered, since a higher grid-point resolution is needed in the trailing-edge regions.

The planform selected for the test cases was the Lockheed wing A wing-body. The wing for this configuration has a quarterchord sweep of 25 deg, a linear twist distribution ranging from 2.28 deg at the wing body junction to -2.04 deg at

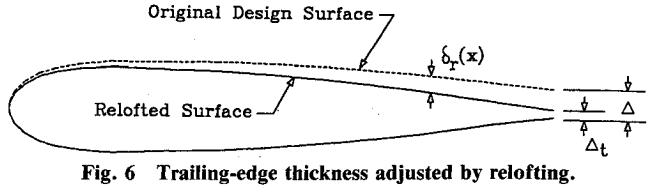

Fig. 6 Trailing-edge thickness adjusted by relofting.

the wing tip, an aspect ratio of 8, and a taper ratio of 0.4. The last two values are based on the wing without fuselage. However, instead of the supercritical sections normally associated with wing A, the initial airfoil sections at each span station were assumed to be composed of symmetric NACA four-digit airfoil sections.

The target pressure distributions used in the design regions for the first test case were selected to yield airfoil shapes thicker in the aft portions of each section and, at supercritical conditions, to yield on the upper surface weaker and more forward shock waves than those that would normally occur on an NACA 0012 section. On the lower surface, the target pressure distributions were selected to have either a favorable pressure gradient or fairly constant pressure plateau over much of the lower surface.

For the second test case, the pressure distribution was obtained from analysis solutions of an assumed wing geometry. The intent of this case is to verify the relofting procedures and show the ability of the current method to make large surface changes in going from a thick wing to a thin wing (approximately 12% to 6% thick, respectively).

Both cases were for a freestream Mach number of 0.8 and an angle of attack of 2 deg. In each case, the pressure distribution was specified in the design regions from the 15% local chord location to the trailing edge and used as the boundary condition in these inverse regions starting with the first iteration. Prior to the first design surface update calculation, 300 SLOR iterations were executed and, subsequently, surface updates were computed every 50 cycles. The solution was considered converged and terminated after 550 total iterations for the first case and, due to the large amount of relofting required, after 950 iterations for the second case.

Test Case I

The inverse design regions for case I, which was an attempt to design both upper and lower surfaces on two noncontiguous regions of the wing at supercritical conditions, are shown in Fig. 7. A comparison between the initial pressure distribution associated with NACA 0012 sections and the target pressures for two of the designed sections is portrayed in Figs. 8 and 9. As can be seen, the target pressure distribution essentially eliminates the upper-surface shock wave present at inboard stations of the original wing; at outboard stations, it weakens the shock and moves it forward. In addition, significant changes in the lower-surface pressure gradients are evident. Also shown in Figs. 10 and 11 are the pressures computed by the program at the end of the inverse design procedure (denoted as "design pressures"). These pressures are in excellent agreement with the target pressures, which indicates that the method is satisfying properly the desired inverse boundary conditions.

The corresponding designed airfoil sections for this case are shown in Figs. 10 and 11. Even on the expanded scale, the agreement between the designed and target surfaces is excellent at all design stations. However, trailing-edge closure

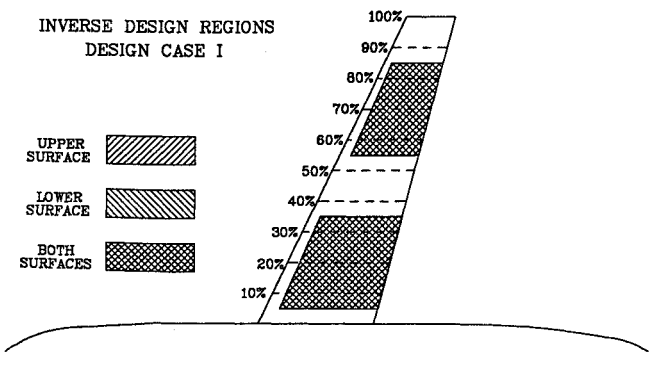

Fig. 7 Design case I.

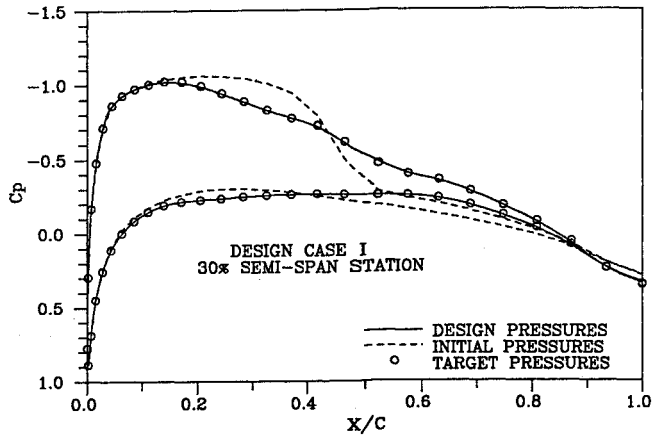

Fig. 8 Comparison of initial pressures with target and final values (case I, 30% station).

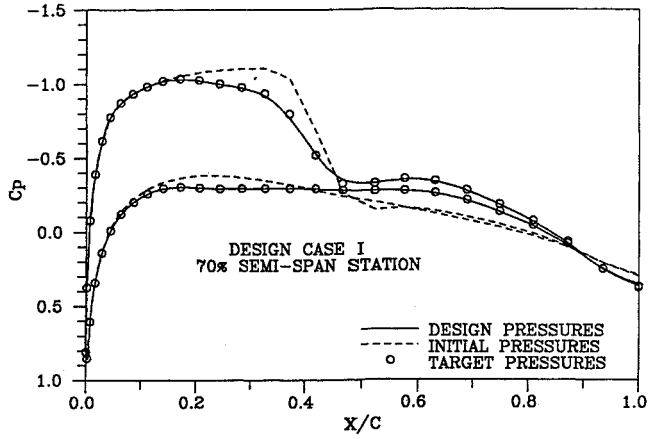

Fig. 9 Comparison of initial pressures with target and final values (case I, 70% station).

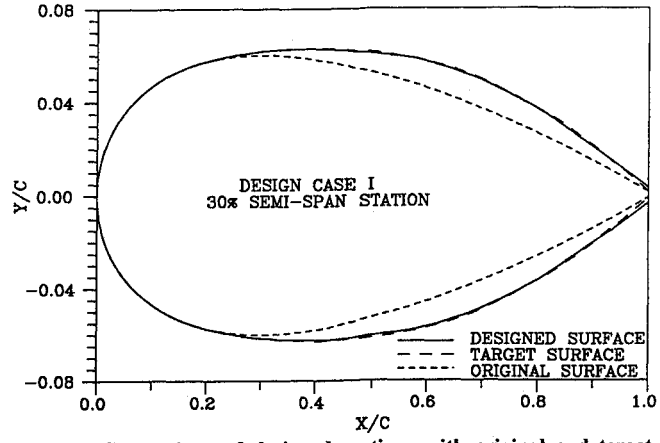

Fig. 10 Comparison of designed sections with original and target sections (case I, 30% station).

was not enforced for this case, and at the boundary stations there is some departure between the designed surfaces and the target surfaces near the trailing edge. It is believed that this slight difference is a ramification of the change in spanwise regions.

In any event, the pressure distributions resulting from an analysis of the designed surface shown in Figs. 10 and 11 are in excellent agreement with the target pressures, as can be seen in Figs. 12 and 13. In addition, the section lift coefficients at the various design stations are in very good agreement with the target coefficients. Based on these results, it is believed that the present method can adequately design/modify nonadjacent regions of a wing in transonic flow.

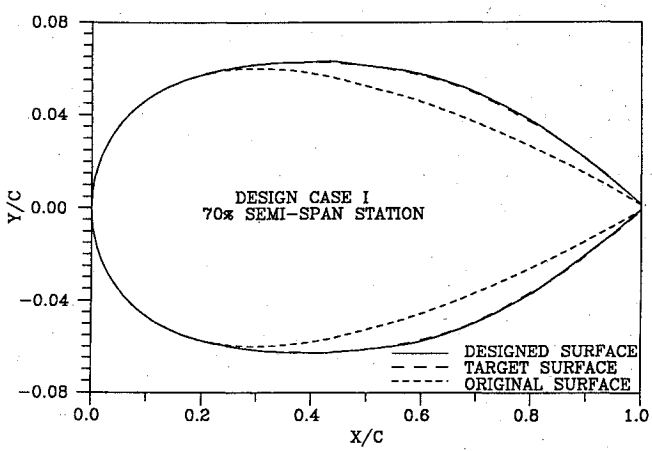

Fig. 11 Comparison of designed sections with original and target sections (case I, 70% station).

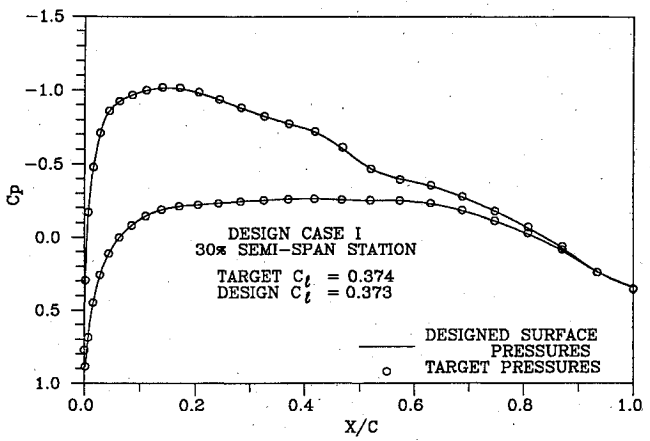

Fig. 12 Comparison of pressures from analysis of designed wing with target pressures (case I, 30% station).

Test Case II

This test case was selected to demonstrate the ability of the design methodology to handle two difficult design tasks. The first task was to change a wing from supercritical to subcritical, which is both a typical engineering task and a significant problem for wing design algorithms. The second task was to make large surface changes to the original airfoil without generating large surface distortions from the accumulation of geometry calculation errors. Due to the upstream dependence of the supersonic flow, this required making large changes in the leading-edge region through the relofting procedures. The design regions for this case are shown in Fig. 14, where the wing thickness varied from 12 to 6% between the wing root and 80% span location, and was constant going outward to the tip. The input design pressures were for a constant 6% thick wing.

The first attempts at this design used the linear leading-edge relofting procedure and from a practical standpoint were unsuccessful. The final design surfaces were still supersonic in the leading-edge regions while satisfying the subsonic aft surface conditions by producing strong shocks at the direct-inverse junction location. In addition, the surfaces themselves had sharp surface slope discontinuities at the same location.

When the thinning approach was used to reloft the leading edge, much better solutions were obtained. Figures 15–26 show the changes in pressure distribution and surface shapes with a comparison of target to designed surface pressures for a few span sections as in the previous case. As can be seen, excellent agreement between target and final pressures and surface were again attained for this extreme case. The only noticeable surface irregularity are a small wiggle at the direct-inverse junction that can be seen as a small pressure wiggle in the pressure plots.

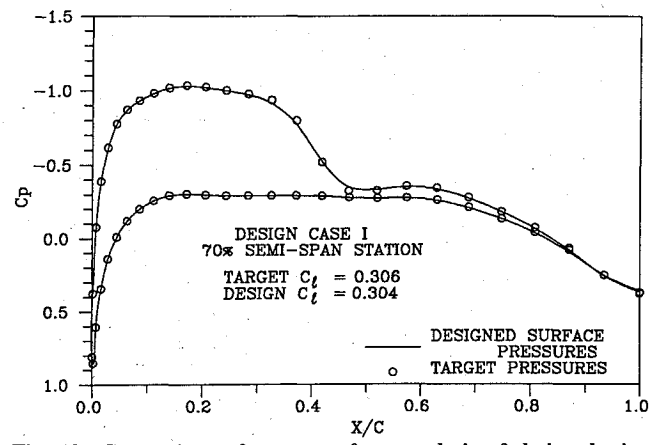

Fig. 13 Comparison of pressures from analysis of designed wing with target pressures (case I, 70% station).

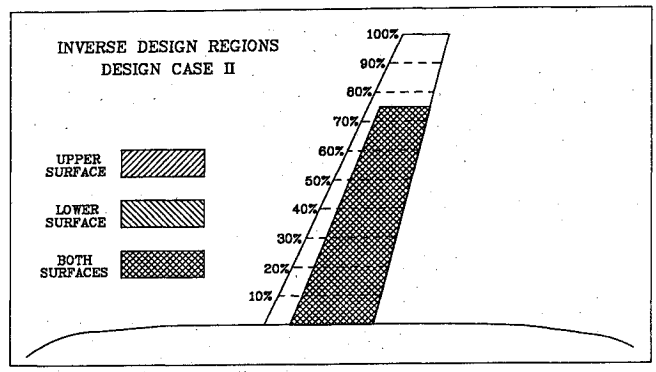

Fig. 14 Design case II.

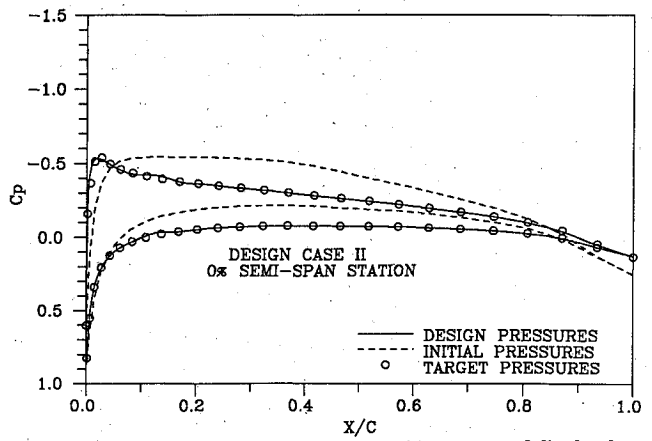

Fig. 15 Comparison of initial pressures with target and final values (case II, 0% station).

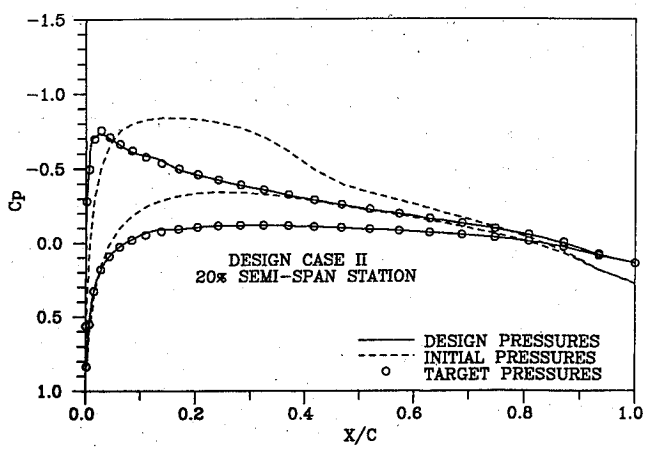

Fig. 16 Comparison of initial pressures with target and final values (case II, 20% station).

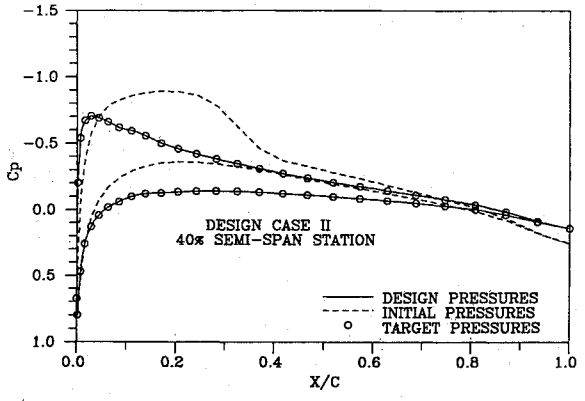

Fig. 17 Comparison of initial pressures with target and final values (case II, 40% station).

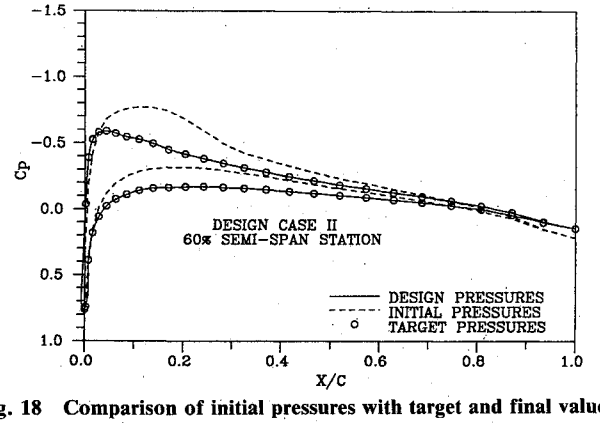

Fig. 18 Comparison of initial pressures with target and final values (case II, 60% station).

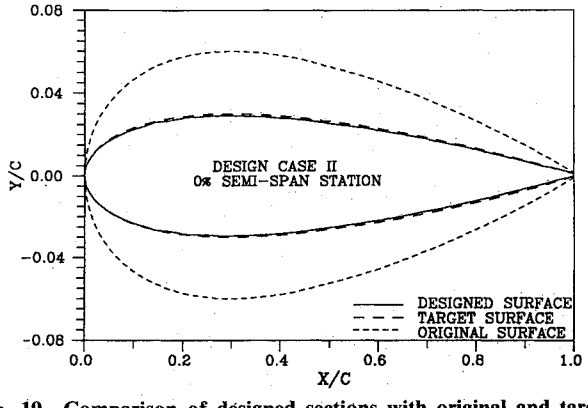

Fig. 19 Comparison of designed sections with original and target sections (case II, 0% station).

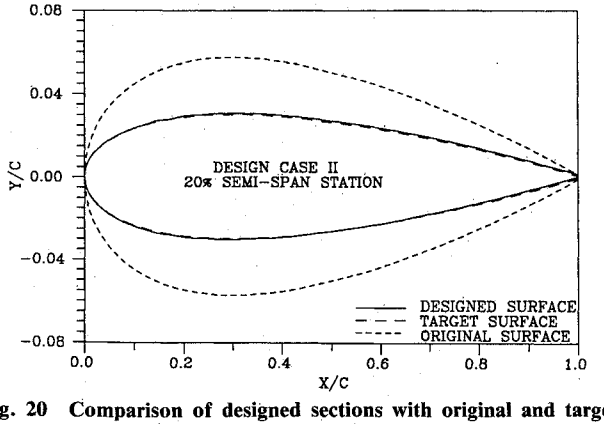

Fig. 20 Comparison of designed sections with original and target sections (case II, 20% station).

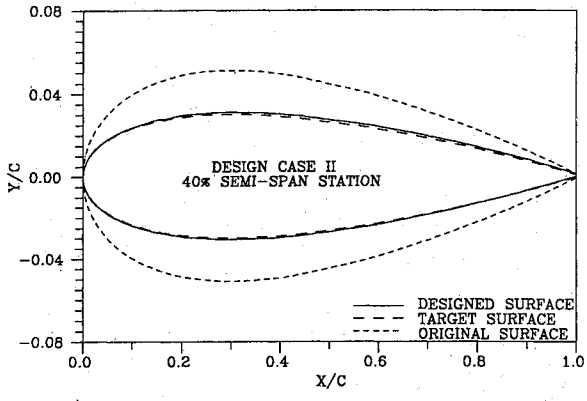

Fig. 21 Comparison of designed sections with original and target sections (case II, 40% station).

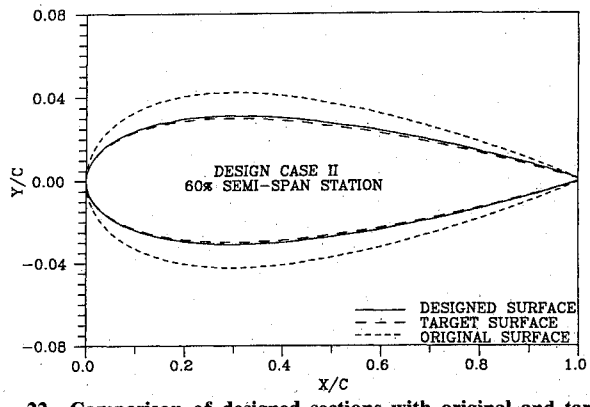

Fig. 22 Comparison of designed sections with original and target sections (case II, 60% station).

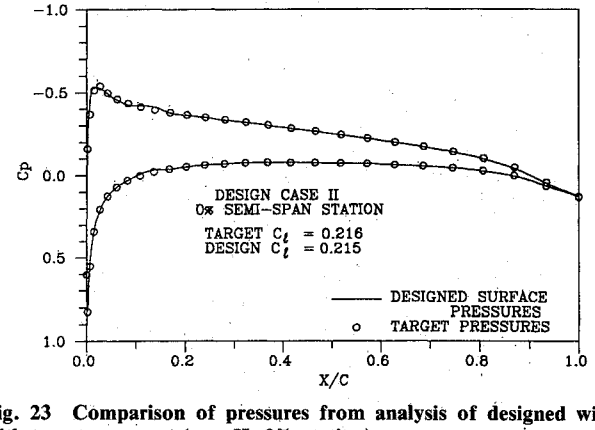

Fig. 23 Comparison of pressures from analysis of designed wing with target pressures (case II, 0% station).

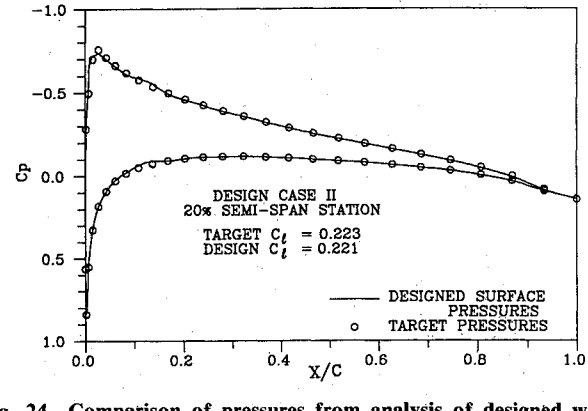

Fig. 24 Comparison of pressures from analysis of designed wing with target pressures (case II, 20% station).

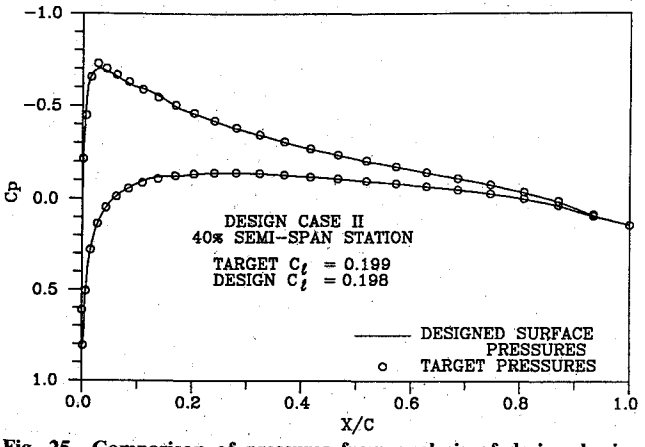

Fig. 25 Comparison of pressures from analysis of designed wing with target pressures (case II, 40% station).

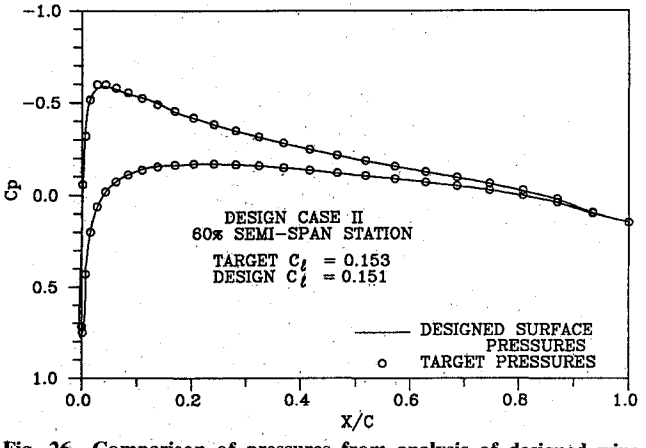

Fig. 26 Comparison of pressures from analysis of designed wing with target pressures (case II, 60% station).

Conclusions

A direct-inverse wing design method has been successfully incorporated into the TAWFIVE transonic wing-body analysis computer code. The resultant code is capable of designing or modifying wings at both transonic and subsonic conditions and includes the effects of wing-body interactions. A series of test cases have been presented that demonstrate the accuracy and versatility of this inverse method. Additional test cases and results are also presented in Refs. 16 and 17.

Acknowledgments

The work presented in this paper was primarily supported by NASA under Grant NAG-1-619 with Richard L. Campbell of the Langley Research Center as technical monitor. The authors express their appreciation to Mr. Campbell and Edgar Waggoner of NASA Langley for their assistance and helpful suggestions.

References

[1]Boppe, C.W., "Transonic Flow Field Analysis for Wing-Fuselage Configurations," NASA CR-3243, May 1980.

[2]Holst, T.L. and Ballhaus, W.F., "Fast, Conservative Schemes for the Full Potential Equation Applied to Transonic Flow," *AIAA Journal,* Vol. 17, Feb. 1979, pp. 145–152.

[3]Caughey, D.A. and Jameson, A., "Progress in Finite-Volume Calculation for Wing-Fuselage Combinations," AIAA Paper 79-1513, July 1979.

[4]Melson, N.D. and Streett, C.L., "TAWFIVE: A User's Guide," NASA TM 84619, Sept. 1983.

[5]Cosentino, G.B. and Holst, T.L., "Numerical Optimization Design of Advanced Transonic Wing Configurations," AIAA Paper 85-0424, Jan. 1985.

[6]Davis, W., "TRO-2D: A Code for Rational Transonic Aero Optimization," AIAA Paper 85-0425, Jan. 1985.

[7]Bauer, F., Garabedian, P., and McFadden, G., "The NYU Inverse Swept Wing Code," NASA CR-3662, Jan. 1983.

[8]Tatsumi, S. and Takanashi, S., "Experimental Verification of Three-Dimensional Transonic Inverse Method," AIAA Paper 85-4077, Oct. 1985.

[9]Carlson, L.A., "Transonic Airfoil Design Using Cartesian Coordinates," NASA CR-2578, April 1976.

[10]Carlson, L.A., "TRANDES: A Fortran Program for Transonic Airfoil Analysis or Design," NASA CR-2821, June 1977.

[11]Anderson, W.K. and Carlson, L.A., "Inverse Transonic Wing Design on a Vector Processor," Texas A&M Research Foundation, TAMRF-4535-8212, Dec. 1982.

[12]Weed, R.A., Anderson, W.K., and Carlson, L.A., "A Direct-Inverse Three-Dimensional Transonic Wing Design Method for Vector Computers," AIAA Paper 84-2156, Aug. 1984.

[13]Jameson, A. and Caughey, D.A., "A Finite Volume Method for Transonic Potential Flow Calculations," *Proceedings of AIAA 3rd Computational Fluid Dynamics Conference*, AIAA, New York, June 1977, pp. 35–54.

[14]Jameson, A., "Iterative Solution of Transonic Flows over Airfoils and Wings, Including Flows at Mach 1," *Communication on Pure and Applied Mathematics,* Vol. 27, 1974, pp. 283–309.

[15]Jameson, A., "Transonic Potential Flow Calculations Using Conservative Form," *Proceedings of AIAA 2nd Computational Fluid Dynamics Conference,* AIAA, New York, June 1975, pp. 148–161.

[16]Gally, T.A. and Carlson, L.A., "Inverse Transonic Wing Design Using Inverse Methods in Curvilinear Coordinates," *5th Applied Aerodynamic Conference*, AIAA, New York, Aug. 1987, pp. 516–526.

[17]Gally, T.A., "Inverse Transonic Wing Design Using Finite-Volume Methods in Curvilinear Coordinates," M.A. Thesis, Texas A&M Univ., College Station, TX, May 1987.